Experimental realization of quantum algorithm for solving linear systems of equations

Jian Pan,[1] Yudong Cao,[2] Xiwei Yao,[3,*] Zhaokai Li,[1] Chenyong Ju,[1,4] Hongwei Chen,[5,†] Xinhua Peng,[1,4] Sabre Kais,[6,7,‡] and Jiangfeng Du[1,4,§]

[1]*Hefei National Laboratory for Physical Sciences at Microscale and Department of Modern Physics, University of Science and Technology of China, Hefei 230026, People's Republic of China*

[2]*Department of Computer Science, Purdue University, West Lafayette, Indiana 47907, USA*

[3]*Department of Electronic Science and Fujian Key Laboratory of Plasma and Magnetic Resonance, School of Physics and Mechanical and Electrical Engineering, Xiamen University, Xiamen, Fujian 361005, China*

[4]*Synergetic Innovation Center of Quantum Information & Quantum Physics, University of Science and Technology of China, Hefei, Anhui 230026, China*

[5]*High Magnetic Field Laboratory, Hefei Institutes of Physical Science, Chinese Academy of Sciences, Hefei 230031, People's Republic of China*

[6]*Department of Chemistry, Physics and Birck Nanotechnology Center, Purdue University, West Lafayette, Indiana 47907, USA*

[7]*Qatar Environment and Energy Research Institute, Qatar Foundation, Doha, Qatar*

(Received 2 June 2013; revised manuscript received 7 November 2013; published 12 February 2014)

Many important problems in science and engineering can be reduced to the problem of solving linear equations. The quantum algorithm discovered recently indicates that one can solve an N-dimensional linear equation in $O(\log N)$ time, which provides an exponential speedup over the classical counterpart. Here we report an experimental demonstration of the quantum algorithm when the scale of the linear equation is 2×2 using a nuclear magnetic resonance quantum information processor. For all sets of experiments, the fidelities of the final four-qubit states are all above 96%. This experiment gives the possibility of solving a series of practical problems related to linear systems of equations and can serve as the basis to realize many potential quantum algorithms.

DOI: 10.1103/PhysRevA.89.022313 PACS number(s): 03.67.Ac, 02.60.−x, 76.60.−k, 85.40.−e

I. INTRODUCTION

Linear equations are omnipresent in nearly all fields of research in science and engineering that involve quantitative analysis. For example, in chemistry, linear equations arise commonly in problems such as electrostatic calculation in density functional theory, where the discretized Poisson equation takes a linear form [1]. In quantum reactive scattering, the Kohn variational calculation involves the inversion of the augmented stiffness matrix, which is equivalent to solving a linear system in certain situations [2]. Also solving linear equations often plays a role as an intermediate step in many algorithms, a typical one of which is data fitting [3]. The algorithm of linear equations of N unknowns for a classical computer, even to obtain an approximate solution, in general requires time that scales at least as N [4]. Hence, any improvement in the cost scaling over this is a significant computational advantage.

Quantum computing has attracted tremendous interest in both the physics and computer science community because of the current progress on developing quantum algorithms [5–7] that outperform their classical counterparts. Recently, Harrow *et al*. [8] proposed a quantum algorithm that is able to solve linear equations $A\vec{x} = \vec{b}$ (A being the N-dimensional Hermitian matrix) in $O(\log N)$ time using $O(\log N)$ qubits, indicating another promising application of quantum computers.

The advantage of the algorithm is confined to cases where one is not interested in $\vec{x}$ itself, but the value of $\vec{x}^\dagger M\vec{x}$ for some quantum mechanical operator M. Thus this algorithm is different from some deterministic quantum algorithms, such as the Deutsch-Jozsa algorithm [9], that provide the solution by a determinate final pure state. Since the value $\langle x|M|x\rangle$ is obtained by a measurement of M with respect to $|x\rangle$, the experiment needs to be carried out multiple times using a pure state but only once on an ensemble system.

With the maturity of the nuclear magnetic resonance (NMR) engineering experience and its well-developed control technology [10], NMR has been used to realize many of the first demonstrations of quantum algorithms [11–13]. In this paper we start by describing the quantum circuit for solving a 2×2 instance of $A\vec{x} = \vec{b}$. Then we show the implementation of the algorithm using a four-qubit NMR quantum information processor. We carried out the experiment for three different vectors $\vec{b}$, and the fidelities of all three final four-qubit states were checked to be above 96%. The algorithm is potentially useful for a range of applications. For example, it could serve as a subroutine for other quantum algorithms such as data fitting [3]. Also, as pointed out in Ref. [8], the algorithm could prove useful in determining certain properties of stochastic processes [14].

II. DESCRIPTION OF THE ALGORITHM

Given any $N \times N$ Hermitian matrix with a spectral decomposition $A = \sum_{j=1}^{N} \lambda_j |u_j\rangle\langle u_j|$, where λ_j is the eigenvalue of A and $|u_j\rangle$ is the corresponding eigenstate, solving the linear system $A\vec{x} = \vec{b}$ is equivalent to finding state $|x\rangle$ that satisfies $A|x\rangle = |b\rangle$. It thus suffices to implement

*yau@xmu.edu.cn
†hwchen@hmfl.ac.cn
‡kais@purdue.edu
§djf@ustc.edu.cn

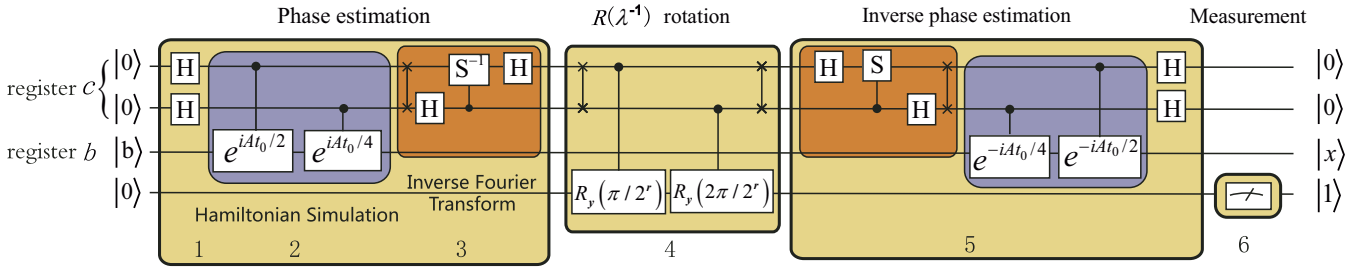

FIG. 1. (Color online) Quantum circuit for implementation of the algorithm in the experiment. Here $r = 2$ and $t_0 = 2\pi$, determining the precision and probability of the correct answer. The matrix forms of the single-qubit gates are $S = \begin{pmatrix} 1 & 0 \\ 0 & i \end{pmatrix}$, $H = \frac{1}{\sqrt{2}}\begin{pmatrix} 1 & 1 \\ 1 & -1 \end{pmatrix}$, $R_y(\theta) = \begin{pmatrix} \cos(\theta/2) & -\sin(\theta/2) \\ \sin(\theta/2) & \cos(\theta/2) \end{pmatrix}$. The vertical segments with "×" mean SWAP operations.

$A^{-1} = \sum_j \lambda_j^{-1}|u_j\rangle\langle u_j|$. By expanding $|b\rangle$ in the eigenbasis of A as $|b\rangle = \sum_j \beta_j|u_j\rangle$, the quantum mechanical solution to the linear system is $|x\rangle \propto A^{-1}|b\rangle \propto \sum_j(\beta_j/\lambda_j)|u_j\rangle$. The main steps of the quantum algorithm are shown in Fig. 1. The first two qubits (termed register c) are used for phase estimation, the third qubit (register b) stores the input vector $\vec{b}$ and the output vector $\vec{x}$, and the fourth is an ancillary qubit which needs to be measured in the end of the circuit.

The initial state is $|b\rangle = \sum_{i=1}^{N} b_i|i\rangle$, expanded in the computational basis together with a few ancilla qubits in $|0\rangle$ states. We then perform the well-known phase estimation algorithm [15] with the controlled unitary operator $U = \sum_{\tau=0}^{T-1}|\tau\rangle\langle\tau| \otimes e^{iA\tau t_0/T}$, where $T = 2^l$, with l being the qubit number of register c. The state of registers c and b after this step is transformed into $\sum_j \beta_j|\lambda_j\rangle_C|u_j\rangle_B$, where $|\lambda_j\rangle$ represents the binary representations of λ_j stored to a precision of t qubits. A crucial step of the algorithm is to introduce an ancilla qubit $|0\rangle$ and then using the $|\lambda_j\rangle$ as a control register to get the state

$$\sum_j \left(\sqrt{1 - \frac{C^2}{\lambda_j^2}}|0\rangle + \frac{C}{\lambda_j}|1\rangle\right)\beta_j|\lambda_j\rangle|u_j\rangle. \qquad (1)$$

Here C is an appropriate constant [16]. To implement this, we first prepare the state $|\theta_j\rangle$ with $\theta_j = 2\arcsin(C/\lambda_j)$ using $|\lambda_j\rangle$, and then use $|\theta_j\rangle$ as the control register to rotate the anxilla qubit by a controlled rotation C-$R_y(\theta_j)$, where $R_y(\theta_j) = e^{-i\theta_j Y}$, with Y being the Pauli operator. It was shown in Ref. [17] that by using quantum circuits to simulate Newton's iteration, the state $|\theta_j\rangle$ approximating θ_j up to an error ε can be prepared with $O[\text{poly}(\log(1/\varepsilon))]$ cost. The final step of the algorithm is to apply the inverse of the previous operations, so as to transform the register c back to $|00\rangle$. When a projective measurement on the ancilla qubit yields $|1\rangle$, the state in register b will collapse to the desired state $\sum_j C\frac{\beta_j}{\lambda_j}|u_j\rangle \propto |x\rangle$ with a probability of $|C^2\sum_j \beta_j^2\lambda_j^{-2}|$, which is shown to scale as $O(1/\kappa^2)$, with κ being the condition number of A [8].

To realize the algorithm experimentally with a limited number of qubits, some simplifications with respect to the general algorithm are necessary. For a four-qubit quantum circuit, instead of using auxiliary qubits, the subroutine for computing λ_j^{-1} can be accomplished by a SWAP gate between the first two qubits $|01\rangle \overset{\text{SWAP}}{\longleftrightarrow} |10\rangle$, which changes $\lambda_1 = 1$ (01 in binary form) into $2\lambda_1^{-1}$ and $\lambda_2 = 2$ (10 in binary form) into $2\lambda_2^{-1}$. Then we use $|2\lambda_j^{-1}\rangle$ states to apply $R_y(\lambda_j^{-1})$ rotation on the ancilla qubit. As shown in Fig. 1, the C-$R_y(\theta_j)$ gates apply rotation with $\theta_j = (2\pi/2^r)\lambda_j^{-1}$, where r is a parameter that influences the error due to the approximation $\sin(\theta_j/2) \approx \theta_j/2$. We generate the state in Eq. (1) by taking $r = 2$ and the corresponding $C = 0.736$ derived from Ref. [16].

Here we take an instance of $A\vec{x} = \vec{b}$ specified by $A = \frac{1}{2}\begin{pmatrix} 3 & 1 \\ 1 & 3 \end{pmatrix}$ and $\vec{b} = \begin{pmatrix} b_1 \\ b_2 \end{pmatrix}$, so that we can perform a precise phase estimation for the two eigenvalues of A that are powers of 2. In principle, the circuit in Fig. 1 can be extended to fit for an arbitrary Hermitian matrix A in a straightforward way.

III. EXPERIMENT

The experiment was carried out on a Bruker AV-400 spectrometer (9.4 T) at 303.0 K. We chose iodotrifluoroethylene dissolved in d-chloroform, where a ^{13}C nucleus and three ^{19}F nuclei constitute a four-qubit quantum system. We label ^{13}C as the first qubit, and $^{19}F_1$, $^{19}F_2$, and $^{19}F_3$ as the second, third, and fourth qubits. Figure 2 shows the measured properties of this four-qubit quantum system. The experiment consists of three parts: (A) pseudopure state preparation, (B) implementation of the quantum algorithm, and (C) state tomography. Figure 3 is the pulse sequence of the experiment.

	^{13}C	F_1	F_2	F_3
^{13}C	15479.7 Hz			
F_1	-297.7 Hz	-33122.4 Hz		
F_2	-275.7 Hz	64.6 Hz	-42677.7 Hz	
F_3	39.1 Hz	51.5 Hz	-129.0 Hz	-56445.8 Hz
T_2^*	1.22 s	0.66 s	0.63 s	0.61 s
T_2	7.9 s	4.4 s	6.8 s	4.8 s

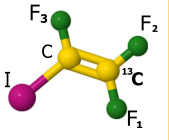

FIG. 2. (Color online) Properties of the iodotrifluoroethylene molecule. The chemical shifts and J-coupling constants (in Hz) are on and below the diagonal in the table, respectively. The chemical shifts are given with respect to reference frequencies of 376.47 MHz (fluorines) and 100.64 MHz (carbons) at 303.0 K. The molecule contains four weakly coupled spin half nuclei which are ^{13}C, $^{19}F_1$, $^{19}F_2$, $^{19}F_3$. The natural abundance of the sample with a single ^{13}C is about 1%.

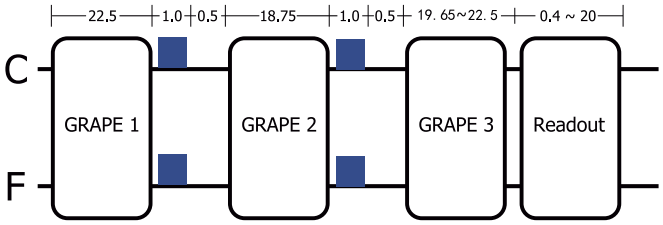

FIG. 3. (Color online) Pulse sequence of the experiment. The numbers that label the pulse symbols represent the time duration of the pulse in milliseconds. The symbols "C" and "F" represent the channels for carbon and fluorine atoms, respectively. The blue rectangular boxes in the figure represent gradient field pulses. The durations of the readout pulses differ from 0.4 to 20 ms.

A. Pseudopure state preparation

This system is first prepared into a pseudopure state (PPS) $\rho_0 = \frac{1-\varepsilon}{16} I + \varepsilon|0000\rangle\langle 0000|$, with I representing the 16×16 unity operator and $\varepsilon \approx 10^{-5}$ the polarization, using the line-selective-transition method [18]. In Fig. 3, the first two gradient ascent pulse engineering (GRAPE) pulses [19] and two gradient field pulses are used to prepare the PPS. The spectrum and state tomography of the pseudopure state are shown in Fig. 4.

B. Implementation of the algorithm

We perform a rotation operation $R_y(\theta) = e^{-iI_y^3\theta}$ (i.e., a rotation along the y axis with an angle θ to the $^{19}F_2$) to obtain the initial state $\rho_{\text{in}} = |00b0\rangle\langle 00b0|$, with the normalized state $|b\rangle = \cos(\theta/2)|0\rangle + \sin(\theta/2)|1\rangle$ representing the state vector $\vec{b} = [\cos(\theta/2), \sin(\theta/2)]^T$. Then, we implement the quantum circuit of the algorithm shown in Fig. 1 on the prepared input state ρ_{in}. All these operations are realized using a shaped radio-frequency (rf) pulse (the third GRAPE pulse in Fig. 3) that is optimized by the gradient ascent pulse engineering (GRAPE) algorithm [19–21]. The GRAPE pulse is characterized by 1500 segments; the pulse duration is about 20 ms and is robust to rf inhomogeneities, with a theoretical fidelity 0.995. Here we consider three different $\vec{b}$ by preparing three input states ρ_{in} with different θ and performing the quantum computation.

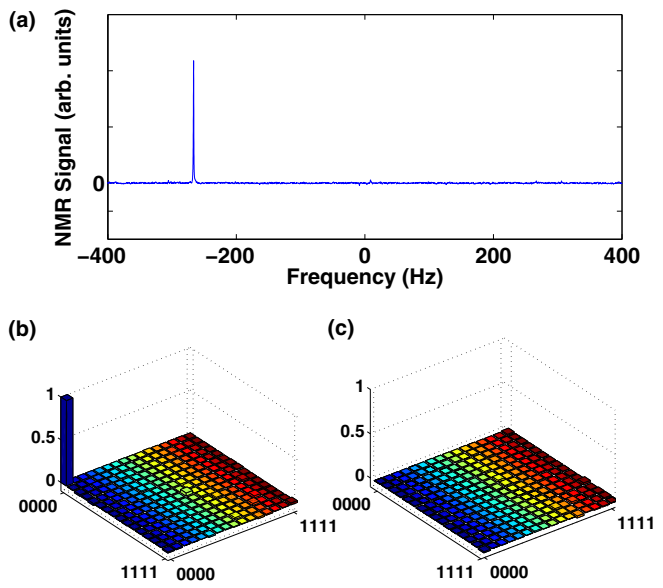

FIG. 4. (Color online) Experimental spectrum and state tomography of the pseudopure state. (a) is the spectrum of ^{13}C obtained by a $\pi/2$ readout pulse. The vertical axes have arbitrary units. (b) and (c) are the real and imaginary parts of the experimentally reconstructed density matrices of the pseudopure state, respectively. The rows and columns in (b) and (c) represent the standard computational basis in binary order, from $|0000\rangle$ to $|1111\rangle$. The fidelity of the whole PPS is 98.73%.

C. State tomography

To examine if the experiments have produced the correction answer, we performed quantum state tomography [22] to the final states. The desired final state shall be in the form $|\Psi_{\text{end}}\rangle = |00\rangle[(a|0\rangle + b|1\rangle)|0\rangle + |x\rangle|1\rangle]$, with $|x\rangle = c|0\rangle + d|1\rangle$ representing the solution $\vec{x} = (x_1 \quad x_2)^T = (c \quad d)^T/C$, where C is the constant (1). Hence, the qubit of interest, i.e., the third qubit, provides the solution when the fourth qubit is measured to be 1. We perform a partial state tomography to get the information about c and d. The experimental ^{13}C spectra are shown in Fig. 5: $|x_1/x_2|^2 = |c/d|^2$ are the ratio of the intensity of the peaks related to $|0001\rangle$ and $|0011\rangle$. We can obtain these ratios from Figs. 5(a)–5(c), which are about 1:2, 3:1, and 1:1, respectively. In addition, the relative phase between x_1 and x_2 can be obtained by the coherence term cd^* or c^*d of qubit 3.

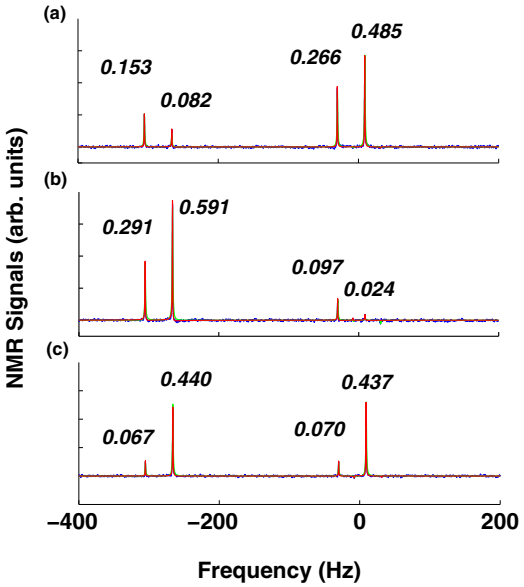

FIG. 5. (Color online) Experimental ^{13}C spectra of the final states after a $\pi/2$ readout pulse for three different $\vec{b}$, which are listed in Fig. 8. There are eight peaks for ^{13}C. Here we only show four of them related to the solution, and their intensities represent the respective probabilities of projecting the final state onto the states $|0011\rangle, |0000\rangle, |0001\rangle, |0010\rangle$ from left to right. The other four peaks are almost zero, which are not shown here. The vertical axes have arbitrary but the same units. The numbers above the peaks are the relative intensity compared to the intensity of the peak of PPS. The experimentally measured, fitting, and ideal spectra are shown as the blue, red, and green curves, respectively.

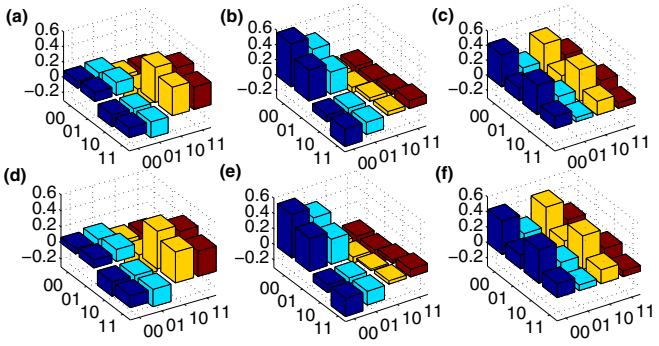

FIG. 6. (Color online) Experimental reconstructed partial density matrices for the final states. (a)–(c) are real parts of experimentally reconstructed density matrices of the final states in the subspace where the first and the second qubits are in the $|00\rangle$ state, along with the theoretical expectations (d)–(f). The rows and columns represent the standard computational basis in binary order, from $|00\rangle$ to $|11\rangle$.

Since A and $\vec{b}$ are both real, $\vec{x}$ is real and the relative phase is either 0 or π determined by the sign of cd^*. There may exist a global phase indeterminable in the solution $\vec{x}$, but this is not relevant for the estimation of the expectation value of some operator associated with $\vec{x}$.

The natural abundance of the sample in which just one carbon is ^{13}C is about 1%. To distinguish those molecules against the large background, we read out all three ^{19}F qubits via the ^{13}C channel, by applying SWAP gates and reading out the ^{13}C qubit. The partial state tomography can be achieved by five readout pulses ($YEEE$, $YEEE * \text{swap}_{12}$, $YEEE * \text{swap}_{13}$, $YEEE * \text{swap}_{14}$, $XEEE * \text{swap}_{13}$; here E represents the unity operator; X and Y represent, respectively, a $\pi/2$ rotation operation along the x and y axis; swap_{ij} denotes a SWAP operation between the ith and jth qubits). The first four readout pulses are to get $|c|^2$ and $|d|^2$, while the last readout pulse is to get the relative phase of c^*d. The real parts of the reconstructed density matrices in the subspace labeled by $|00\rangle_{12}$ are shown in Fig. 6. Furthermore, we perform the complete quantum state tomography [22] (which needs 44 readout pulses) for the final state in the Hilbert space spanned by all four qubits as shown in Fig. 7. We list all the results of the three experiments in Fig. 8, with the experimental fidelities being all above 96%. The state fidelity is calculated by using $F = \text{Tr}(\rho_{\text{alg}}\rho_{\text{exp}})/\sqrt{\text{Tr}(\rho_{\text{alg}}^2)\text{Tr}(\rho_{\text{exp}}^2)}$, where ρ_{exp} and ρ_{alg} represent the experimentally measured density matrix and the corresponding ideal algorithm expectation.

IV. DISCUSSION

The infidelity of the experimental final state, i.e., its deviation from the ideal algorithm expectation of the algorithm, is about 3%–4%. It is well known that inhomogeneity of magnetic fields, the imperfection of the GRAPE pulses, the variations of the chemical shift, and decoherence are sources of infidelity. Numerical simulations reveal that the imperfection of the GRAPE pulses produces about a 1% error to the final state, which can cause about a 2% error to the intensities of some peaks. The infidelity due to decoherence is estimated to be about 1.5% from the experimental time of 50 ms and the coherence time 0.61–1.22 s given in Fig. 2. Another source of error comes from state tomography. Numerical simulations [23] show that the decoherence effect on the state readout will cause at most an error of 0.3% to the fidelity of the final state. To reduce the error due to the noise in the spectra, fitting with the Lorentzian function was adopted to obtain the intensity of the peaks.

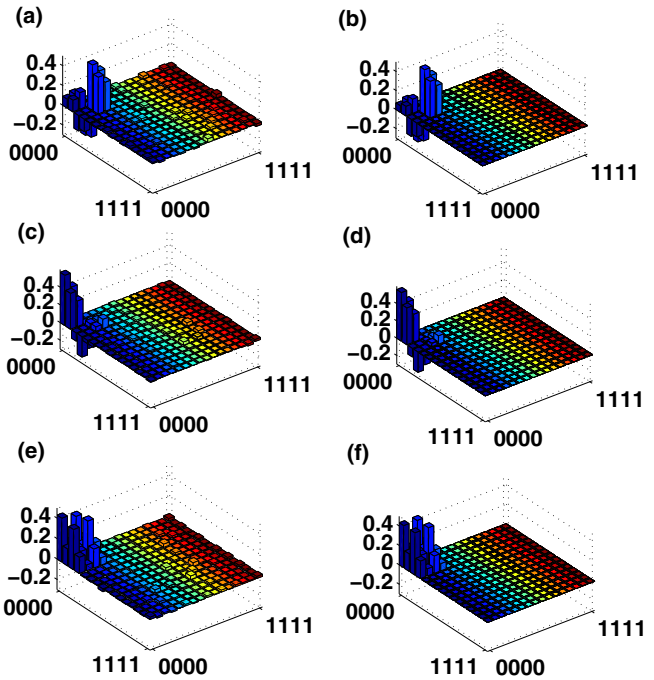

FIG. 7. (Color online) Experimental final state tomography. (a), (c), and (e) are the real parts of the state tomography of the experimental final states for experiments 1, 2, and 3, respectively, along with the theoretical expectations (b), (d), and (f). The rows and columns represent the standard computational basis in binary order, from $|0000\rangle$ to $|1111\rangle$. The fidelities of the experimental final states are 96.4%, 96.6%, and 96.7%, respectively.

Exp. No.	θ (*rad*)	$\vec{b}$	$\vec{x}_{\text{theory}}$	$\vec{x}_{\text{alg}}$	$\vec{x}_{\text{exp}}$	$\lvert\Delta x_i\rvert_{\text{max}}^{\text{theory}}$	$\lvert\Delta x_i\rvert_{\text{max}}^{\text{alg}}$	$\lvert\Delta x_i\rvert_{\text{max}}$	Fidelity
1	−2.23	$\begin{pmatrix}0.439\\-0.898\end{pmatrix}$	$\begin{pmatrix}0.554\\-0.784\end{pmatrix}$	$\begin{pmatrix}0.523\\-0.762\end{pmatrix}$	$\begin{pmatrix}0.556\\-0.737\end{pmatrix}$	0.05	0.03	0.03	96.4%
2	−0.57	$\begin{pmatrix}0.957\\-0.289\end{pmatrix}$	$\begin{pmatrix}0.790\\-0.456\end{pmatrix}$	$\begin{pmatrix}0.772\\-0.425\end{pmatrix}$	$\begin{pmatrix}0.731\\-0.442\end{pmatrix}$	0.06	0.04	0.03	96.6%
3	1.57	$\begin{pmatrix}0.707\\0.707\end{pmatrix}$	$\begin{pmatrix}0.354\\0.354\end{pmatrix}$	$\begin{pmatrix}0.368\\0.368\end{pmatrix}$	$\begin{pmatrix}0.330\\0.369\end{pmatrix}$	0.02	0.04	0.01	96.7%

FIG. 8. (Color online) Experimental results of the quantum algorithm for solving the linear equations $A\vec{x} = \vec{b}$. $\vec{x}_{\text{theory}}$ is the theoretical solution, $\vec{x}_{\text{alg}}$ is the ideal solution obtained by the algorithm, and $\vec{x}_{\text{exp}}$ is the experimental solution obtained by quantum state tomography. Here $|\Delta x_i|_{\text{max}}^{\text{theory}} = |x_{\text{exp}}^i - x_{\text{theory}}^i|_{\text{max}}$, $|\Delta x_i|_{\text{max}}^{\text{alg}} = |x_{\text{exp}}^i - x_{\text{alg}}^i|_{\text{max}}$, and $|\Delta x_i|_{\text{max}} = |x_{\text{alg}}^i - x_{\text{theory}}^i|_{\text{max}}$, where x_{exp}^i, x_{theory}^i, and x_{alg}^i are the ith elements of $\vec{x}_{\text{exp}}$, $\vec{x}_{\text{theory}}$, and $\vec{x}_{\text{alg}}$, respectively. The fidelity in the table refers to the final state of the whole four-qubit system, and is measured between the experimental final state and the ideal algorithm expectation.

There are intrinsic approximations in the algorithm, i.e., the phase estimation in the second step and the control-rotation operation in the fourth step shown in Fig. 1, which will bring deviation to the experimental solution $\vec{x}_{\text{exp}}$ from the theoretical expectation $\vec{x}_{\text{theory}}$. The eigenvalues of A chosen in our experiment satisfy $\lambda_k = \frac{2\pi k}{t_0}$, and so the phase estimation is perfect and contains no error in theory [8]. The error due to control-rotation operation depends on the quality of the approximation $\sin\alpha \approx \alpha$, where α is the rotation angle which is an integral multiple of $\frac{\pi}{2^{r+1}}$ acted on the ancillary qubit. The theoretical error in this step decreases as r increases, while the intensities of the counterpart peaks of the final states are proportional to $\frac{1}{r^2}$. Here, we adopted a balanced choice $r = 2$ in the experiment. The resultant theoretical error on $|\Delta x_i|_{\text{max}}$ is about 3% (given in Fig. 8), and the intensities of the counterpart peaks are about 10% of the intensity of PPS.

V. CONCLUSION

In summary, we experimentally demonstrate the quantum algorithm for solving linear systems of equations in a four-qubit NMR system. We acquire solutions with errors of about 7% for all three experimental implementations, which show fine experimental accuracy and the validity of the algorithm. The experimental demonstration of the algorithm sheds light on many potential applications. For example, the ability to use the quantum algorithm to solve the Poisson equation [17] would allow quantum chemists to speed up electrostatic calculations in density function theory. Since the quantum algorithm could be used efficiently for solving linear systems of differential equations [24], a quantum computer might prove to be useful in solving differential equation systems that arise in various technical applications. Furthermore, the algorithm can serve as a basis to realize a series of quantum algorithms related to linear equations [3].

Note added: Related results were obtained by two other groups using other systems [25,26].

ACKNOWLEDGMENTS

This work was supported by the National Key Basic Research Program of China (Grants No. 2013CB921800 and No. 2014CB848700), the National Natural Science Foundation of China (Grants No. 11227901, No. 91021005, No. 11375167, No. 11004181, and No. 11161160553), and the Strategic Priority Research Program (B) of the CAS (Grant No. XDB01030400). S.K. thanks the NSF Center for Quantum Information and Computation for Chemistry for support under Award No. CHE-1037992.

[1] R. G. Parr and W. Yang, *Density-Functional Theory of Atoms and Molecules*, Vol. 16 (Oxford University Press, Oxford, UK, 1989).
[2] R. D. Levine, *Quantum Mechanics of Molecular Rate Processes* (Dover, New York, 1999).
[3] N. Wiebe, D. Braun, and S. Lloyd, Phys. Rev. Lett. **109**, 050505 (2012).
[4] G. H. Golub and C. F. van Loan, *Matrix Computation* (John Hopkins University Press, Baltimore, MD, 1996).
[5] P. Shor, in *Proceedings of the 35th Annual Symposium on Foundations of Computer Sciience*, edited by S. Goldwasser (IEEE, New York, 1994), pp. 124–134.
[6] S. Lloyd, Science **273**, 1073 (1996).
[7] L. K. Grover, in *Proceedings of the 28th Annual ACM Symposium on Theory of Computing* (ACM, New York, 1996), pp. 212–219.
[8] A. W. Harrow, A. Hassidim, and S. Lloyd, Phys. Rev. Lett. **103**, 150502 (2009).
[9] D. Deutsch, Proc. R. Soc. London, Ser. A **400**, 97 (1985).
[10] C. A. Ryan, C. Negrevergne, M. Laforest, E. Knill, and R. Laflamme, Phys. Rev. A **78**, 012328 (2008).
[11] I. L. Chuang, L. M. Vandersypen, X. Zhou, D. W. Leung, and S. Lloyd, Nature (London) **393**, 143 (1998).
[12] J. A. Jones, M. Mosca, and R. H. Hansen, Nature (London) **393**, 344 (1998).
[13] E. Knill, R. Laflamme, R. Martinez, and C.-H. Tseng, Nature (London) **404**, 368 (2000).
[14] P. Valiant, SIAM J. Comput. **40**, 1927 (2011).
[15] M. A. Nielsen and I. L. Chuang, *Quantum Computation and Quantum Information* (Cambridge University Press, Cambridge, UK, 2000).
[16] Y. Cao, A. Daskin, S. Frankel, and S. Kais, Mol. Phys. **110**, 1675 (2012).
[17] Y. Cao, A. Papageorgiou, I. Petras, J. Traub, and S. Kais, New J. Phys. **15**, 013021 (2013).
[18] X. Peng, X. Zhu, X. Fang, M. Feng, K. Gao, X. Yang, and M. Liu, Chem. Phys. Lett. **340**, 509 (2001).
[19] N. Khaneja, T. Reiss, C. Kehlet, T. Schulte-Herbrüggen, and S. J. Glaser, J. Magn. Reson. **172**, 296 (2005).
[20] D. Lu, N. Xu, R. Xu, H. Chen, J. Gong, X. Peng, and J. Du, Phys. Rev. Lett. **107**, 020501 (2011).
[21] N. Xu, J. Zhu, D. Lu, X. Zhou, X. Peng, and J. Du, Phys. Rev. Lett. **108**, 130501 (2012).
[22] J.-S. Lee, Phys. Lett. A **305**, 349 (2002).
[23] L. M. Vandersypen, M. Steffen, G. Breyta, C. S. Yannoni, M. H. Sherwood, and I. L. Chuang, Nature (London) **414**, 883 (2001).
[24] D. W. Berry, arXiv:1010.2745.
[25] S. Barz, I. Kassal, M. Ringbauer, Y. O. Lipp, B. Dakic, A. Aspuru-Guzik, and P. Walther, arXiv:1302.1210.
[26] X.-D. Cai, C. Weedbrook, Z.-E. Su, M.-C. Chen, M. Gu, M.-J. Zhu, L. Li, N.-L. Liu, C.-Y. Lu, and J.-W. Pan, Phys. Rev. Lett. **110**, 230501 (2013).